

Hidden IR structures in NGC 40: signpost of an ancient born-again event

J.A. Toalá¹★, G. Ramos-Larios², M.A. Guerrero³ and H. Todt⁴

¹*Instituto de Radioastronomía y Astrofísica (IRyA), UNAM Campus Morelia, Apartado postal 3-72, 58090 Morelia, Michoacan, Mexico*

²*Instituto de Astronomía y Meteorología, Depto. de Física, CUCEI, Universidad de Guadalajara, Av. Vallarta 2602, Arcos Vallarta, 44130 Guadalajara, Mexico*

³*Instituto de Astrofísica de Andalucía (IAA-CSIC), Glorieta de la Astronomía S/N, 18008 Granada, Spain*

⁴*Institute for Physics and Astronomy, Universität Potsdam, Karl-Liebknecht-Str. 24/25, D-14476 Potsdam, Germany*

1 March 2019

ABSTRACT

We present the analysis of infrared (IR) observations of the planetary nebula NGC 40 together with spectral analysis of its [WC]-type central star HD 826. *Spitzer* IRS observations were used to produce spectral maps centred at polycyclic aromatic hydrocarbons (PAH) bands and ionic transitions to compare their spatial distribution. The ionic lines show a clumpy distribution of material around the main cavity of NGC 40, with the emission from [Ar II] being the most extended, whilst the PAHs show a rather smooth spatial distribution. Analysis of ratio maps shows the presence of a toroidal structure mainly seen in PAH emission, but also detected in a *Herschel* PACS 70 μm image. We argue that the toroidal structure absorbs the UV flux from HD 826, preventing the nebula to exhibit lines of high-excitation levels as suggested by previous authors. We discuss the origin of this structure and the results from the spectral analysis of HD 826 under the scenario of a late thermal pulse.

Key words: stars: evolution — stars: winds, outflows — stars: carbon — infrared: ISM — ISM: molecules — planetary nebulae: individual: NGC 40

1 INTRODUCTION

Planetary nebulae (PNe) are formed as a result of the last gasps in the life of low- and intermediate-mass stars ($M_i \lesssim 8 M_\odot$). Previously, these stars have evolved to become asymptotic giant branch stars (AGB) that eject large amounts of mass into their circumstellar medium through dense and slow winds to finally reach the post-AGB phase where they develop fast stellar winds and strong ionising photon flux. The wind-wind interaction creates an inner cavity while the UV flux from the central star photoionises the material, creating a PN (e.g., Balick 1987).

The PN NGC 40 around the hydrogen deficient star HD 826 presents a variety of morphological features that uncover the different stages of mass ejection in the formation of PNe. As shown in the colour-composite picture presented in Figure 1, the nebula has a barrel-like main cavity whose northern and southern caps open into a set of lobes or blisters, sometimes associated with jets, although there is not kinematical evidence of fast outflows (see, e.g., Meaburn et al. 1996). A set of optical and IR concentric rings surround the main cavity (Corradi et al. 2004; Ramos-Larios et al. 2011), disclosing the last gasps in the AGB of HD 826, the central star of NGC 40. The main nebula is surrounded by an extended filamentary structure, probably associated with heavy mass-loss events

during the AGB, whose morphology seems to suggest that the nebula is interacting with the interstellar medium (ISM) due to its relatively high velocity (Martin et al. 2002).

The nebula exhibits a large C/O ratio, as derived from abundance determinations based on collisionally excited lines (e.g., Pottasch et al. 2003). This is in line with the carbon-rich [WC8]-type of its central star (Crowther et al. 1998). Furthermore, the *ISO* IR nebular spectrum also shows the ~ 21 and $30 \mu\text{m}$ broad emission features detected in many C-rich AGB and PNe (see Forrest et al. 1981; Sloan et al. 2014; Mishra et al. 2015; Sloan 2017, and references therein), which can be associated with a carbon-rich chemistry, including polycyclic aromatic hydrocarbon (PAH) clusters, hydrogenated amorphous carbon grains, hydrogenated fullerenes, nanodiamonds and unidentified carbonaceous material (Ramos-Larios et al. 2011). Detailed modelling of the PAH species in NGC 40 has been recently presented by Boersma et al. (2018).

Spectral fits to optical and UV spectroscopic observations of HD 826 based on NLTE models agree that its effective temperature should be $T_{\text{eff}} \approx 90 \text{ kK}$ (Bianchi & Grewing 1987; Leuenhagen et al. 1996; Marcolino et al. 2007). However, the nebula presents low excitation, with the [O II] $\lambda 3727$ doublet being the strongest feature in the optical spectrum (e.g., Pottasch et al. 2003). Rough estimates based on the Zanstra and Stoy methods or even highly sophisticated estimates using photo-ionisation models point to an effective temperature $T_{\text{eff}} \lesssim 40 \text{ kK}$ (Köppen & Tarafdar

★ E-mail: j.toala@irya.unam.mx

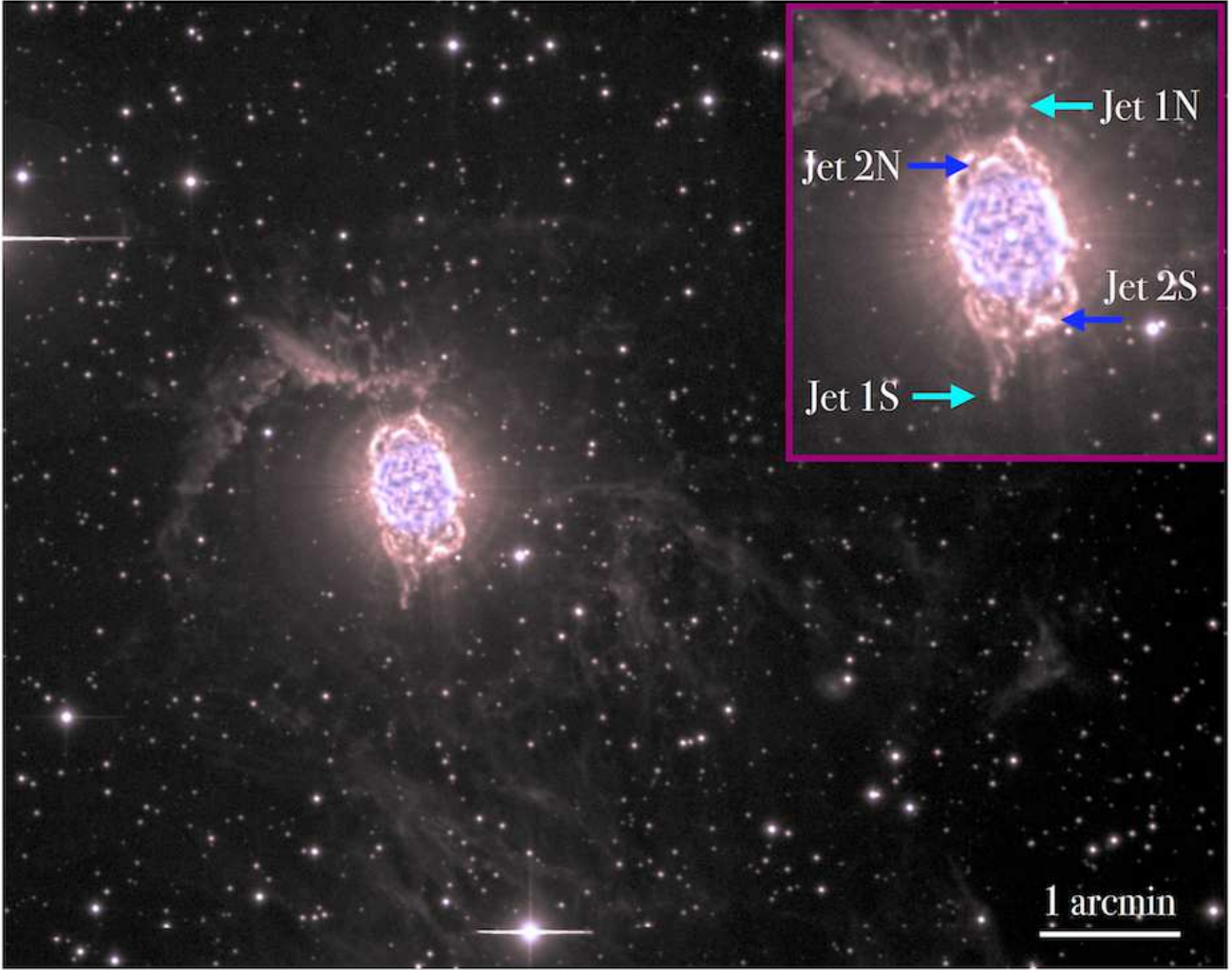


Figure 1. Isaac Newton Telescope (INT) Wide-Field Camera (WFC) colour-composite picture of NGC 40. Red and green correspond to the $H\alpha+[N II]$ emission and blue is $[O III]$. The inset shows a close-up of the main nebula around HD 826, the central star of NGC 40, in which we have labelled the main jet-like features identified by Meaburn et al. (1996). Images courtesy of R.L.M. Corradi. North is up, east to the left.

1978; Preite-Martinez & Pottasch 1983; Harman & Seaton 1966; Pottasch et al. 2003; Monteiro & Falceta-Gonçalves 2011). In order to explain this discrepancy, Bianchi & Grewing (1987) proposed the existence of a carbon-rich *curtain* around HD 826. These authors argue that the absorption features seen in the resonance transition of the $C II \lambda\lambda 1334.5, 1335.7$ doublet detected in *IUE* observations imply a dense, carbon-rich circumstellar envelope around HD 826 expanding at a velocity lower than its terminal wind velocity ($V_\infty \approx 1000 \text{ km s}^{-1}$; Guerrero & De Marco 2013).

In this paper we use *Spitzer* IRS observations obtained in map mode, *Herschel* PACS $70 \mu\text{m}$, and Canada-France-Hawaii Telescope (CFHT) images to assess the spatial distribution of ionic species, PAHs, H_2 , and dust in the central region of NGC 40. The comparison of their distributions indeed unveils the presence of structures inside the main cavity of NGC 40 close to the central star that may partially block its UV flux. The paper is organized as follows. We describe the observations used here in Section 2 and present our main results on the spatial distribution of different components in Section 3. We discuss these results and present a

possible origin for these structures in Section 4. Finally, a summary of our findings and conclusions is given in Section 5.

2 OBSERVATIONS

We use here *Spitzer* Space Observatory observations of NGC 40 (program ID 50834, AORKey 29685248; PI: D. Weedman) obtained on 2009 March 8. These correspond to Infrared Spectrograph (IRS) observations performed in map mode using the short-low (SL) slits covering the spectral range from 5.2 to $14.5 \mu\text{m}$. Up to 160 slit positions were placed on the main nebular cavity of NGC 40 (see Figure 2), with another 160 slit positions for background subtraction. The combination of the 160 slits onto NGC 40 cover an angular area of $\sim 64'' \times 60''$. The pixel scale of the SL detector is $1''8^1$.

The IRS data were processed using the CUbe Builder for IRS

¹ <https://irsa.ipac.caltech.edu/data/SPITZER/docs/irs/irsinstrumentation>

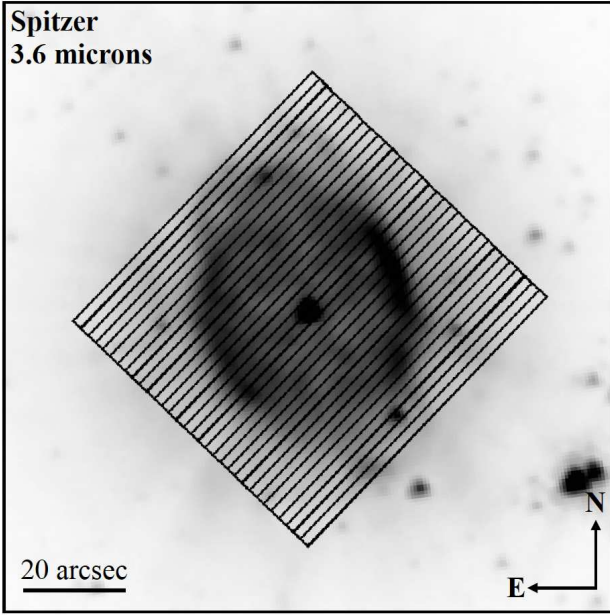


Figure 2. Slit coverage of the *Spitzer* IRS observations of NGC 40 overlaid on the *Spitzer* IRAC 3.6 μm image.

Spectra Maps (CUBISM; Smith et al. 2007). CUBISM was used to visualize spectral maps and to obtain spectra from different regions within NGC 40, as well as an integrated spectrum. Standard characterization of noise, background subtraction, and bad bixel removal procedures were followed.

To supplement the *Spitzer* spectral maps of NGC 40, we also analysed *Spitzer* IRAC and *Herschel* PACS observations. The *Spitzer* IRAC observations correspond to the program ID 40115 (AORKey 21976576; PI: G. Fazio) obtained on 2007 October 17, whereas the *Herschel* PACS data correspond to the observation ID 1342223905 (PI: T. Ueta) obtained on 2011 July 10. All observations were downloaded from the NASA/IPAC Infrared Science Archive². We have also used near-IR CFHT observations of NGC 40 obtained with the Wide-field InfraRed Camera (WIRCam) through the *K* broadband ($\lambda_c=2.146 \mu\text{m}$, $\Delta\lambda=0.325 \mu\text{m}$) and H_2 1-0 narrowband ($\lambda_c=2.122 \mu\text{m}$, $\Delta\lambda=0.032 \mu\text{m}$) filters on 2008 July 18 (PI: P. Martin).

We also obtained UV and optical observations of HD 826 to model its spectrum and estimate its stellar properties (see Discussion section). HD 826 was observed by the *Far Ultraviolet Spectroscopic Explorer* (*FUSE*) and the *International Ultraviolet Explorer* (*IUE*) satellites. Data from these observations have been retrieved from MAST, the Multimission Archive at the Space Telescope Science Institute³. We used the *FUSE* observations with Obs. ID A08501010000 and A08501020000 (PI: H. Dinerstein) obtained on 2000 December 16 in the spectral range 916–1190 \AA with total exposure times of 15 and 26 ks.

For the *IUE* spectral range of 1230–1980 \AA and 1900–3220 \AA only low dispersion spectra were available. We used the *IUE* datasets with Obs. ID SWP03074 and LWR02656, both taken with the large

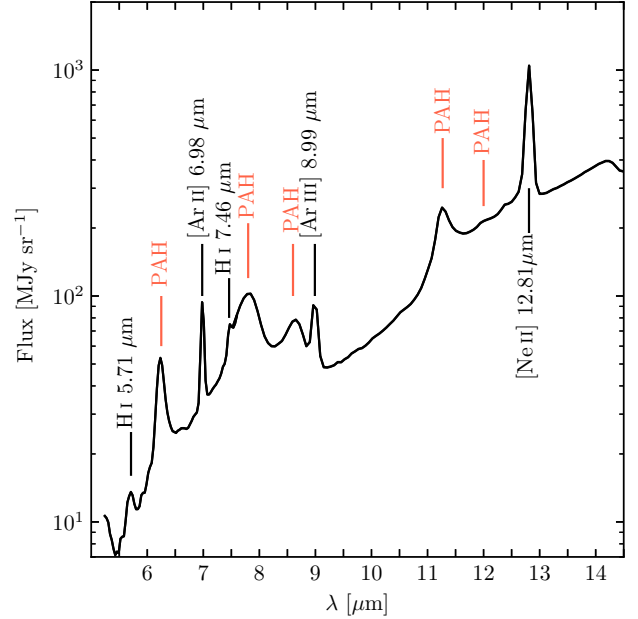


Figure 3. *Spitzer* IRS low-resolution background-subtracted spectrum of NGC 40. The spectrum includes emission from all the SL slits shown in Fig. 2. Broad line emission attributed to PAHs are marked at 6.3, 7.7, 8.6, 11.3, and 12.0 μm . Other prominent emission lines from ionised species are marked.

aperture with total exposure times of 480 s for each pointing. Finally, we obtained high-resolution Fibre-fed Echelle Spectrograph (FIES) observations at the Nordic Optical Telescope (NOT). The observations were obtained on 2015 December 11 on service mode using the high-resolution fibre, which gives a resolution of $R = 67000$ for the 3640–9110 \AA wavelength range. The total FIES exposure time was 900 s.

3 RESULTS

Figure 3 presents the integrated background-subtracted *Spitzer* IRS spectrum of NGC 40. The spectrum was built adding all the emission coming from the nebular regions covered by the IRS slits as shown in Fig. 2. The spectrum exhibits the clear presence of PAHs at 6.2, 7.7, 8.6 and 11.3 μm , as well as a small contribution of the 12.0 μm feature (see also figure 2 in Boersma et al. 2018). The spectrum shows notable emission features from low ionisation species such as [Ar II] at 6.98 μm , [Ar III] at 8.99 μm , and [Ne II] at 12.81 μm . A few weak H I emission lines are also present. In agreement with Ramos-Larios et al. (2011), no H_2 emission lines are detected in the 5–14 μm spectral range.

The *Spitzer* IRS observations presented here provide us the opportunity to study the spatial distribution of the emission from the different PAHs and low-ionisation emission lines detected in the integrated spectrum of NGC 40. To perform this study, we used CUBISM to create spectral maps centred at the lines of the low-ionisation species and broad emission features of PAHs (see Figure 3). For all maps, we subtracted the local continuum following the procedure described in Smith et al. (2007). We do not show the spectral map of the 7.7 μm PAH feature because it lays at the edge between the two nodes of the SL orders. For completeness, we also extracted a continuum image for the wavelength range between 13–14 μm ,

² <http://irsa.ipac.caltech.edu/Missions/spitzer.html>

³ STScI is operated by the Association of Universities for Research in Astronomy, Inc., under NASA contract NAS5-26555.

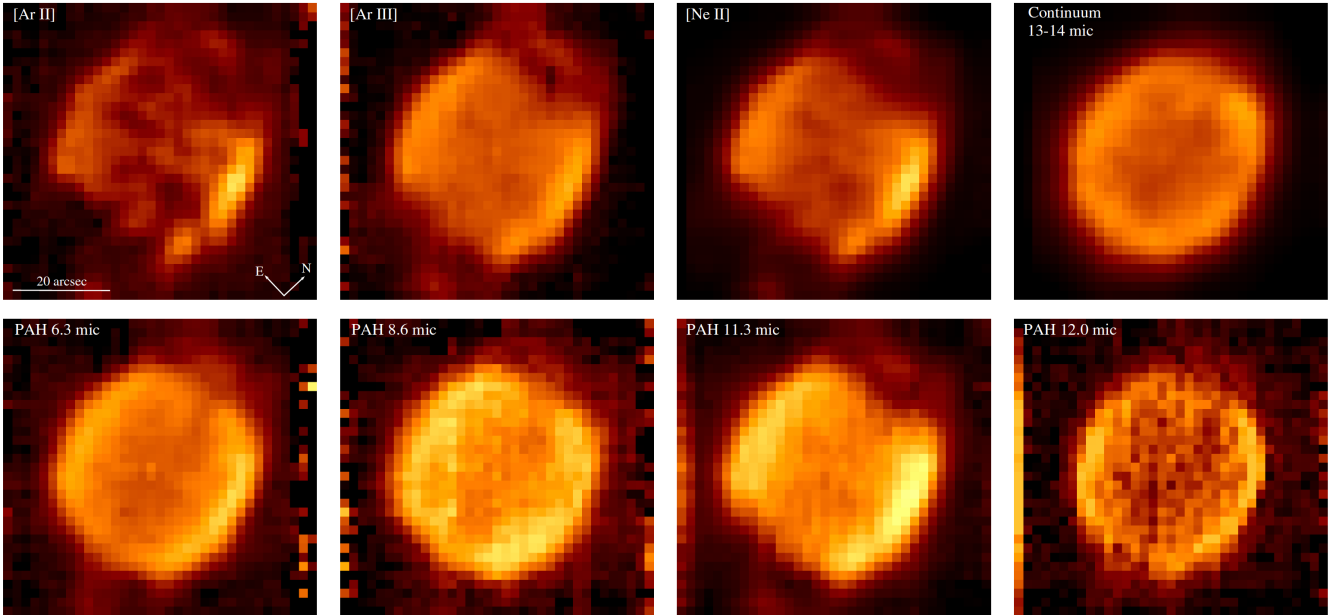


Figure 4. Spatial maps extracted for different spectral features. The top-right panel shows a continuum image corresponding to the emission-free 13–14 μm spectral range. All panels have the same field of view and orientation.

with no contribution from any line or PAH feature. For simplicity, we labelled this spectral image as “continuum”. All spectral maps are shown in Figure 4.

The spectral maps of the ionic species resemble the optical images presented in Figure 1: a clumpy barrel-like main cavity with two blobs aligned N-S just outside this cavity, which are spatially coincident with the optical blobs or blisters. The [Ar II], [Ar III], and [Ne II] spectral maps present a limb-brightened morphology along the minor axis of NGC 40, with emission peaking towards the west. In contrast, the continuum image presents an elliptical shape with a limb-brightened morphology with no apparent contribution to any other morphological feature.

The spatial distribution of the emission in the PAH spectral maps shares some of the properties of that of the emission lines from ionised species, although some differences are noticeable. The PAH emission also shows a limb-brightened morphology, with brighter emission as well in the western region for the 6.3 and 11.3 μm features, but not for the 8.6 and 12 μm ones. Note, however, that the emission from the PAHs seems more uniform within the main cavity than that from the ionised emission lines, particularly for the PAHs at 6.3, 8.6, and 11.3 μm (see Fig. 4 bottom panels). Otherwise, the northern and southern blobs in the PAH spectral maps are located closer to the inner cavity than those in the ionic species, but those in the 11.3 μm PAH feature, which are spatially coincident.

To illustrate the distribution of the ionic species, the continuum and the PAHs features, we present colour-composite images combining different spectral maps in the top panels of Fig. 5. The top-left panel shows the comparison of the three ionic spectral maps. This image clearly reveals the clumpy morphology of the emission in the [Ar II] and [Ne II] lines, as well as the extent of the blowouts north and south of the barrel-like main nebula. The top-middle panel compares the distribution of the PAHs. Although the emission in the 6.3, 8.6, and 11.3 μm seems distributed rather uniformly inside the main cavity, the northern and southern edges of the barrel-like structure show noticeable differences. The top-right panel compares

the continuum emission with those of the [Ar II] emission line and PAH feature at 11.3 μm . The dust continuum dominates the emission towards the northern and southern blowouts of the main cavity in NGC 40.

The bottom row panels in Figure 5 present normalised intensity spatial profiles extracted from the spectral maps shown in Fig. 4 along the E-W direction (i.e., $\text{PA}=90^\circ$) for those same spectral features included in the colour-composite pictures of the top row. The bottom-left panel confirms that the [Ar II] emission is more extended towards the east than that of the [Ar III] and [Ne II] emission lines. The variations of the [Ar II] emission in the inner cavity reflect the clumpy structure unveiled by its spectral map as shown in Fig. 4. The comparison of the PAH profiles in the middle-bottom panel shows that the PAH at 11.3 μm is more extended towards the west and is very similar in shape to that of the 6.3 μm PAH feature. These profiles generally have a higher valley to peak ratio than those of the ionised emission lines in the bottom-left panel. The peaks of the 8.6 μm PAH lay just inside the other two profiles. Finally, the bottom-right panel implies the continuum profile has the highest valley to peak ratio, the peaks are the broadest, and they peak inside those of the PAH and emission lines from ionised species. The emission from the 11.3 μm PAH feature is very similar in shape to that of the [Ar III] emission, which is likely to be the position of the photodissociated region in NGC 40. Moreover, we note that the [Ar II] ionic emission encompasses that from the PAHs at 11.30 μm .

Figure 5 hints at the presence of structural components inside the main cavity of NGC 40. In order to highlight this spatial feature, we investigated different ratio maps using the PAHs, continuum and ionic species maps. Interestingly, the PAH ratios unveil a wide structure inside the main cavity in NGC 40 extending from east to west with a width $\sim 30''$. A similar structure can also be appreciated when comparing the PAHs with the continuum map. We show in Figure 6 the PAH 11.3/continuum and PAH 11.3/6.3 ratio images. A dark lane seems to decrease the ratio maps at the middle plane

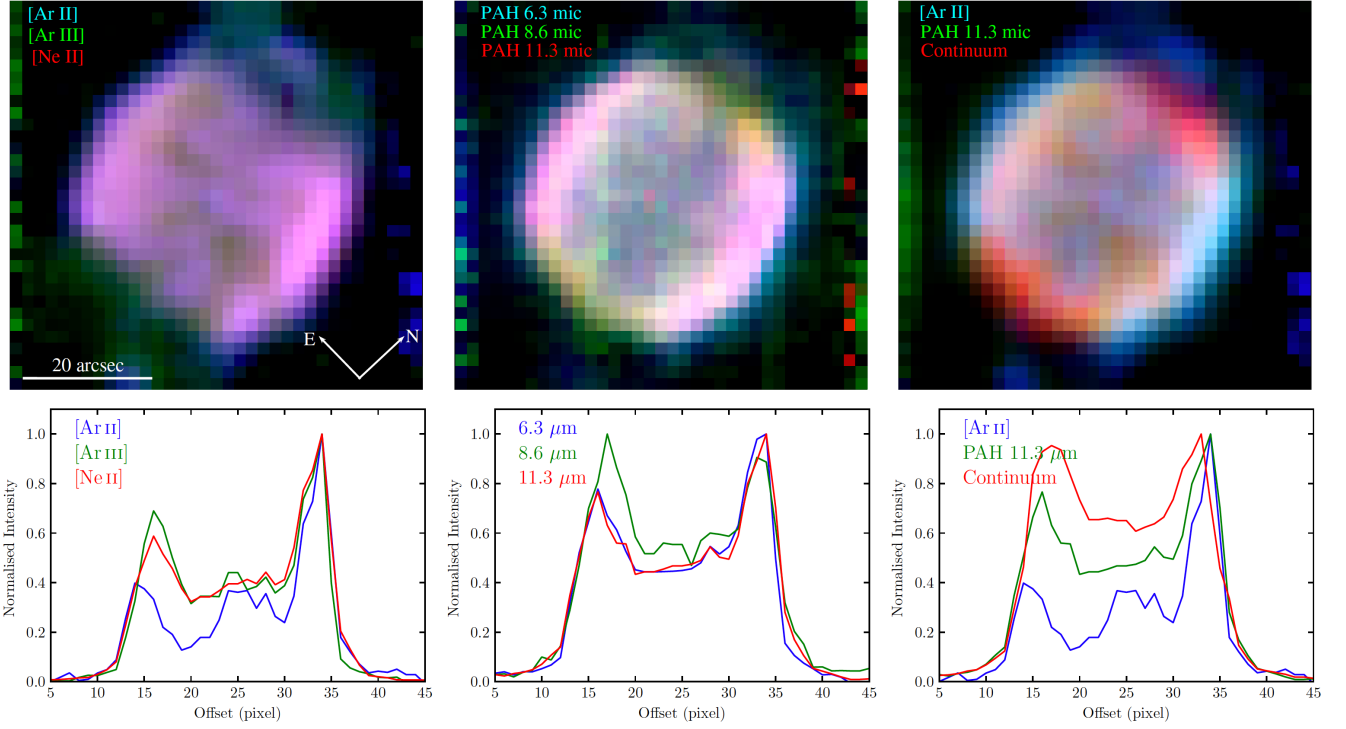


Figure 5. The top panels present colour-composite pictures of NGC 40 combining different spectral images. The bottom panels show normalised intensity profiles of the different spectral maps shown in Fig. 4 extracted along the E-W direction (PA=90°).

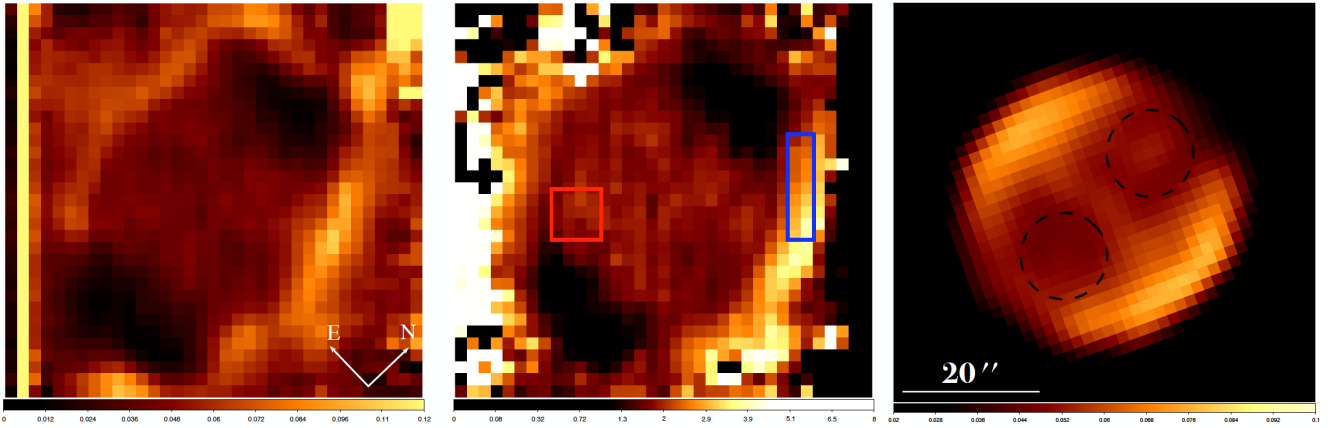


Figure 6. Spectral map ratios of the PAH 11.3 μm feature versus the continuum (left) and the PAH 6.30 μm feature (middle). The panels have the same field of view and orientation as those in Figures 4 and 5. The red and blue boxes overplotted on the middle panel indicate the apertures used to extract the torus and rim spectra shown in Figure 8. The right panel shows the *Herschel* PACS 70 μm image of the same field of view of the other panels. The contrast of the *Herschel* 70 μm image has been chosen to enhance the structures inside the main cavity in NGC 40. The (dashed-line) circles highlight the location of the two blobs of enhanced emission.

from east to west⁴. This structure is detected in emission in the *Herschel* 70 μm image presented in Fig. 6 right panel. We note that

this structure is also easily spotted in the PAH ratio maps presented by Boersma et al. (2018). In addition to brighter emission at the equatorial region, this image unveils the presence of two blobs.

⁴ Similar ratio maps have been created using the continuum-subtracted ionic line ([Ar II], [Ar III] and [Ne II]) maps in order to search for differences in ionisation structure but these images are dominated by clumpy emission and the ration maps are not conclusive.

A wide-field image of the *Herschel* PACS 70 μm is presented in Figure 7 in comparison with other colour-composite IR images of NGC 40. It is interesting to note that the CFHT near-IR images (Fig. 7 right panel) show that H₂ is not present in the main cavity,

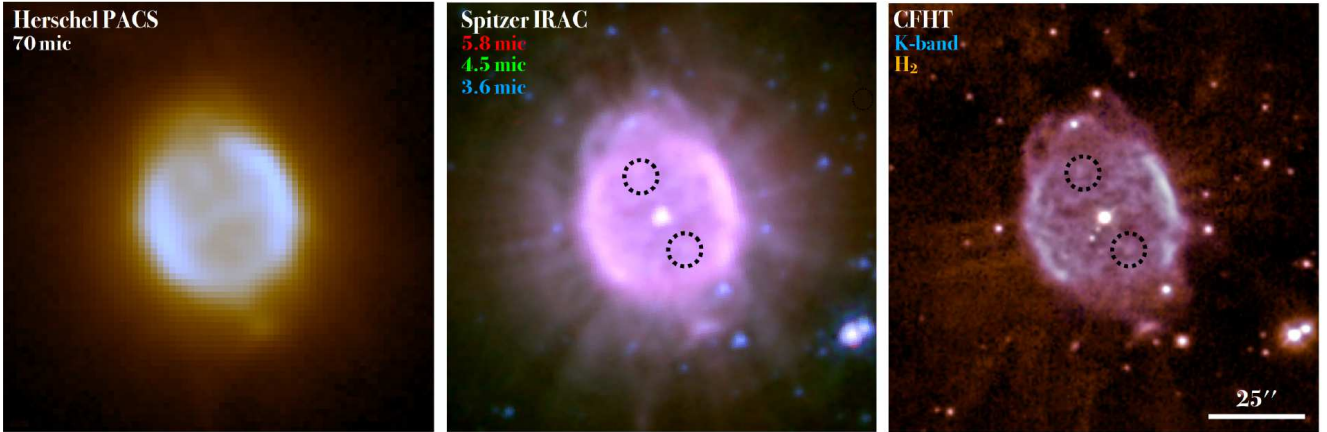


Figure 7. Colour-composite IR images of NGC 40. Left: *Herschel* PACS 70 μm shown at different scales (red - logarithmic, green - square root, blue - linear). Center: *Spitzer* IRAC image. Right: CFHT WIRCam near-IR image. The circular regions in the top-central and -right panels show the position of the two blobs unveiled in the *Herschel* PACS 70 μm image (see also Fig. 6 right panel). The *Herschel* and *Spitzer* bottom images have been processed to enhance the extended emission.

but its emission can be traced as rays protruding from it and along the equatorial (East-West) plane.

A detailed analysis of the IR spectral energy distribution (SED) of the different morphological features of NGC 40 would be desirable, but the available data in the *Herschel* PACS Spectroscopy Catalogue (Ramos-Medina et al. 2018)⁵ cannot spatially resolve NGC 40. The spatial location of continuum emission and the dominant emission line in the PACS 70 μm range, the [O I] 63.2 \AA emission line at cannot be determined. Future SOFIA observations will be used to spatially resolve the toroidal structure around HD 826, to construct detailed SED at longer wavelengths, and to further constrain the properties of these structures in NGC 40.

4 DISCUSSION

Boersma et al. (2018) reported the clear presence of PAH emission around HD 826, the central star of NGC 40, although they reckon there is no obvious substructure in their PAH charge maps. The detailed comparison of *Spitzer* and *Herschel* mid-IR images and ratio maps of NGC 40 shown in Fig. 6 shows it might be interpreted as a toroidal structure inside its ionised shell. Whereas its detection in *Herschel* PACS 70 μm images is indicative of a dust component, the *Spitzer* ratio maps reveal an important content of PAHs, i.e., carbonaceous molecules. It is worthwhile to emphasize that the spatial location of PAHs in NGC 40 does not follow the typical stratified distribution of material seen in photo-dissociation regions, where it is associated with dense knots and the presence of other molecules such as H₂ (see the case of NGC 6720 presented by Cox et al. 2016). Neither it compares with the toroidal structures reported in PNe with dual-dust or mixed chemistry, i.e., PNe with carbon- and oxygen-rich dust (see, e.g., Guzmán-Ramírez et al. 2014). In those cases, the tori have notable ionisation gradients, with ionised species in the innermost regions and PAHs in their outer edges, as the result of the formation of PAHs by photodissociation of CO (Guzmán-Ramírez et al. 2011).

There is additional evidence of the presence of large amounts

of dust and carbon-rich material between HD 826 and the ionised material of NGC 40. First, the morphology of this IR feature in NGC 40 is similar to the emission map of the C IV $\lambda\lambda 1548, 1551$ \AA UV emission lines in the image through the *UVIT* Sapphire filter presented by Kameswara Rao et al. (2018). Then, the low ionisation degree of the PAHs in NGC 40 points to a high internal attenuation, up to $A_V \gtrsim 20$ mag (Boersma et al. 2018). This is in sharp contrast with the extinction derived from the Balmer decrement derived from nebular emission lines or the dip at $\lambda 2200$ \AA seen in UV spectra of the central star, which imply $A_V \approx 1.2$ (see Pottasch et al. 2003, for a through discussion on this issue). Finally, we note the different mid-IR spectra of the toroidal structure and the barrel-shaped nebular rim of NGC 40 (Figure 8). The spectrum of the latter flattens at longer wavelengths, whilst that of the toroidal structure, closer in shape to the total nebular spectrum, rises up, indicating a larger content of dust and molecules. This interpretation confirms the differential spectral results presented by Boersma et al. (2018).

4.1 NLTE analysis of HD 826

Such dusty, carbon-rich toroidal structure would absorb the hard UV flux from the central star of NGC 40, i.e., it would be the carbon *curtain* proposed by Bianchi & Grewing (1987) to explain the discrepancy between the high effective temperature of HD 826 and the anomalously low excitation of the nebula around it. This discrepancy has been questioned by studies modelling the nebular emission, suggesting that the true temperature of HD 826 is lower, down to 38,000 K (Pottasch et al. 2003) or 50,000 K (Monteiro & Falceta-Gonçalves 2011). To confirm the discrepancy between the effective temperature of HD 826 and the nebular excitation of NGC 40, we have analysed public UV (*FUSE* and *IUE*) and optical FIES NOT spectra of HD 826 using the updated version of the Potsdam Wolf-Rayet (PoWR)⁶ NLTE code to produce a detailed atmospheric model (Gräfener et al. 2002; Hamann & Gräfener 2004). Additional details on the computing methods can be found in Todt et al. (2015) and references therein.

⁵ <https://throes.cab.inta-csic.es/>

⁶ <http://www.astro.physik.uni-potsdam.de/PoWR>

The synthetic spectrum was corrected for interstellar extinction due to dust by the reddening law of [Seaton \(1979\)](#), as well as for interstellar line absorption for the Lyman series in the UV range.

For the terminal velocity v_∞ , we obtained a value of 1000 ± 100 km s⁻¹ from the width of the UV P-Cygni line profiles (cf. Fig. 9). A microturbulence velocity of about 100 km s⁻¹ provides the additional line broadening needed to fit the observed emission line profiles. The stellar mass was set to a typical value for CSPNe, $M_* = 0.6 M_\odot$ (see e.g. [Miller Bertolami & Althaus 2007](#)), though we note that the value of M_* has no noticeable influence on the synthetic spectrum. The density contrast between a wind with clumps and a smooth wind of the same mass-loss rate, the so-called micro-clumping parameter D , was derived to have a value of 10 from the fitting of the extended electron scattering wings of strong emission lines (e.g. [Hillier 1991](#); [Hamann & Koesterke 1998](#)).

It was not possible to fit consistently the *FUSE*, *IUE* and optical photometric data. While the *IUE* spectra and optical photometry imply a reddening of $E_{B-V} = 0.41$ mag, the *FUSE* and *IUE* spectra suggest a higher reddening of 0.6 mag and a higher stellar luminosity of $\log(L_*/L_\odot) = 4.45$ that would overestimate the optical flux. The *IUE* observations from different epochs were checked for variability, but no significant differences were found for the well-exposed SWP03075LL (1978-10-20), SWP19081RL (1983-01-25), and SWP53124LL (1994-12-19) observations. Other *IUE* observations seemed to be underexposed or not centred on the central star. Similar issues may affect some of the *FUSE* observations, thus we rely on the well-exposed *IUE* observations and optical photometry to adopt an E_{B-V} of 0.41 mag and $\log(L_*/L_\odot) = 3.85$. This corresponds to $A_V = 1.27$, similar to what was obtained by [Pottasch et al. \(2003\)](#).

The best-fit parameters of our NLTE model of HD 826 are listed in Table 1. The stellar temperature can be constrained by the relative strengths of the emission lines of different ions of the same element, e.g., He I vs. He II or C III vs. C IV. For a given stellar temperature and chemical composition, the equivalent width of any emission line is largely determined by the ratio between the volume emission measure of the wind and the area of the stellar surface, which can be expressed in terms of the transformed radius R_t

$$R_t = R_* \left[\frac{v_\infty}{2500 \text{ km s}^{-1}} / \frac{\dot{M} \sqrt{D}}{10^{-4} M_\odot \text{ yr}^{-1}} \right]^{2/3}, \quad (1)$$

originally introduced by [Schmutz et al. \(1989\)](#). In this equation D is the micro-clumping parameter which is defined as the density contrast between wind clumps and a smooth wind of the same mass-loss rate.

Our best-fit model is compared to the optical and UV spectra in Fig. 9, while the SED of HD 826 is shown in Fig. 10. The resultant effective temperature of our best-fit, $T_{\text{eff}} = 70.8$ kK (as also derived by [Marcolino et al. 2007](#)), confirms the hot status of HD 826 and our estimate for the Zanstra temperature is 45 kK. Although [Crowther et al. \(2003\)](#) determined a higher temperature of 90 kK, we find that such temperature results in C III emission lines much weaker than those observed. Moreover, the [Leuenhagen et al. \(1996\)](#) models result in a too strong iron-forest between 1600–2000 Å and too strong C III emission lines.

[Leuenhagen et al. \(1996\)](#) and [Marcolino et al. \(2007\)](#) reported a carbon mass-fraction of 50% in the atmosphere of HD 826, whereas [Crowther et al. \(2003\)](#) found it to be lower, $\approx 40\%$. We tested different carbon mass-fractions and found them to range between 30% and 50% are consistent with the observations, as most lines are not very sensitive to the carbon mass-fraction rel-

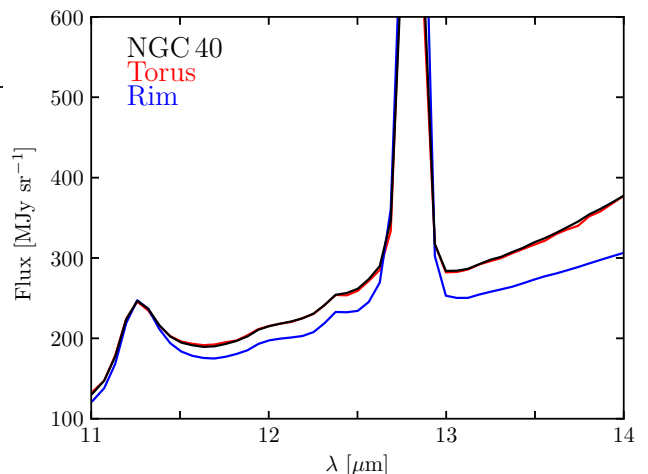


Figure 8. Comparison of the spectrum extracted from NGC 40 (see Fig. 3) with spectra extracted from the bright rim of NGC 40 and a region spatially coincident with the torus structure shown in Fig. 6 right panel. The spectra are normalised to the 11.3 μm feature of the NGC 40 spectrum.

ative to the overall quality of the fit. The diagnostic line-pair He II 5411 / C IV 5471 implies a C:He abundance ratio of 30:67, but the strength of the C III 5696 emission line suggests a higher carbon abundance of 50%. We conclude that a C:He abundance ratio of 40:57 gives a good compromise fit. A solar value for X_N gives a good fit to the nitrogen lines in the high resolution FIES optical spectrum, while a nitrogen abundance of 1.4×10^{-3} by mass results in too strong emission lines. These results confirm [Marcolino et al. \(2007\)](#) estimate for the nitrogen abundance of $< 0.1\%$. The Balmer lines of hydrogen are blended with He II lines, thus the upper limit of 2% of hydrogen by mass estimated by [Leuenhagen et al. \(1996\)](#) cannot be confirmed. As the spectral lines of neon are all blended with other lines, only an upper limit for the neon abundance can be provided, which is also not very strict, given the poor quality of the *IUE* observations. We notice the absence of a strong F VI 1140 line, which is compatible with a solar fluorine abundance. Similarly, phosphorus, sulfur, and silicon solar abundances provide a good fit to the P, S, and Si UV and Si optical spectral lines.

4.2 On the origin of the carbon-rich curtain

The origin of the inner PAH toroidal structure in NGC 40 is intriguing. Whereas the large nebular C/O ratio ([Pottasch et al. 2003](#)) suggests that the central star underwent the third dredge-up, bringing the resultant ¹²C to the stellar surface and turning it into a carbon-rich [WC] star ([Herwig 2005](#)), an eruptive process ejecting carbon-rich material inside the ionised nebular shell seems more likely. [Herwig \(2001\)](#) discussed several scenarios for the formation of [WC]-type central stars of PNe through the *late thermal pulse* (LTP) event. During this event, hydrogen-deficient, carbon-rich material is ejected from the central star inside the old hydrogen-rich PN. This material coagulates rapidly into carbon-rich dust due to the reduction of the effective temperature of the central star. Interestingly, the spatial distribution of the hydrogen-poor ejecta detected in born-again PNe is generally described as disrupted disks and bipolar ejections (e.g., [Borkowski et al. 1994](#); [Evans et al. 2006](#)).

It is thus possible that the central star of NGC 40 experienced a LTP, which ejected carbon-rich material preferentially along an

Table 1. Parameters of the central star from analysis with PoWR.

Parameter	Value	Comment
T_{eff} [kK]	71	
d [kpc]	1.9	from Bailer-Jones et al. (2018)
$\log(L_*/L_{\odot})$	3.85	
R_* [R_{\odot}]	0.56	
R_t [R_{\odot}]	3.55	
D	10	density contrast
$\log(\dot{M}/M_{\odot} \text{ yr}^{-1})$	-6.1	for $D=10$
v_{∞} [km s $^{-1}$]	1000	
v_D [km s $^{-1}$]	100	
M_* [M_{\odot}]	0.6	adopted
$T_{\text{Zanstra}}(\text{H I})$ [kK]	45	
$\log Q(\text{H I})$	47.7	
$\log Q(\text{He I})$	46.9	
$\log Q(\text{He II})$... [†]	
Chemical abundances (mass fraction)		
He	0.57 ± 10	
C	0.40 ± 10	
O	0.03 ± 2	
N	$(6.9 \pm 4) \times 10^{-4}$	solar
Si	6.7×10^{-4}	solar
P	5.8×10^{-6}	solar
S	3.1×10^{-4}	solar
F	4.6×10^{-7}	solar
Ne	< 0.03	
H	< 0.02	
Fe	1.4×10^{-3}	iron group elements, solar

[†] no He II ionising photon escapes the wind, a black body model of same temperature and radius would give $\log_{10} Q(\text{He II}) = 46$. Solar abundances are taken from [Asplund et al. \(2009\)](#).

equatorial plane. As HD 826 came back to the post-AGB track and developed a new fast stellar wind, this material formed dust grains which are now just pushed away into a toroidal structure reaching the edge of the barrel-like main cavity. Thus, the X-ray emission from NGC 40 detected by *Chandra* (see [Montez et al. 2005](#)) might have an identical origin as that of the born-again PNe A 30 and A 78. In such cases, the carbon-rich material interacts with the adiabatically-shocked bubble created by the current fast wind, lowering its temperature to produce diffuse soft X-ray emission ([Guerrero et al. 2012](#); [Fang et al. 2014](#); [Toalá et al. 2015](#)). Furthermore, the carbon *curtain* blocks a significant fraction of the UV flux from HD 826, resulting in the anomalously low ionisation degree of the nebular shell. Similar situation has been recently reported in HuBi 1, a PN whose central star has experienced a very late thermal pulse (VLTP) and the carbon-rich dusty ejecta has obscured the star to a degree such that the outer hydrogen-rich nebular shell has cooled down and started recombining ([Guerrero et al. 2018](#)). The atmosphere of HD 826 consists mostly of He and C, with solar nitrogen and neon abundances and a likely presence of residual hydrogen. These chemical abundances, as expected from stellar evolution models (e.g. [Althaus et al. 2005](#)), favor a LTP event rather than a VLTP one ([Todt & Hamann 2015](#)).

Finally, we would like to mention the presence of several pairs of jet-like ejections in NGC 40, including those unveiled by the *Herschel* PACS 70 μm image (see Figures 6 - right panel and Fig. 7). The most extended are those reported by [Meaburn et al. \(1996\)](#), labelled as Jet 1 in Fig. 1) and the bipolar structure just outside the barrel-like main cavity in NGC 40 (Jet 2 in Fig. 1). Fast collimated ejections are

a typical signature of born-again PNe (see, e.g., [Fang et al. 2014](#), and references therein). The pair of blobs inside the main cavity of NGC 40 (marked in Fig. 7 with dashed-line circular apertures) could also be interpreted as collimated outflows. Their identification in optical or near-IR images has been hampered so far due to the dominant clumpy structure of this PN.

5 SUMMARY

We presented an IR study of NGC 40 around the [WC]-type star HD 826. The *Spitzer* IRS low-resolution spectrum of NGC 40 between 5 and 14 μm confirms its low level of ionisation, as no emission lines from high ionisation species are detected in this spectrum. The main IR spectral features are emission lines from low-ionisation species, such as [Ar II], [Ar III], and [Ne II], and PAH clusters at 6.2, 7.7, 8.6, 11.3, and 12.0 μm . No H₂ emission lines are detected in this spectrum, but the CFHT WIRC*am* H₂ image unveils the presence of molecular hydrogen just outside the main cavity.

The analysis of IR observations of NGC 40 uncovered structures inside the inner cavity of NGC 40. The detection of these structures in *Spitzer* IRS PAH ratio maps and a *Herschel* PACS 70 μm image seems to imply a high content of dust and carbon-rich material. Notably, the structures can be traced in UV C IV images. The morphology of these emissions suggests that a toroidal structure surrounds HD 826.

The current available IR observations suggest that a dusty carbon-rich toroidal structure is embedded inside the optical nebular shell of NGC 40. This toroidal structure around HD 826 would absorb its UV flux, as originally suggested by [Bianchi & Grewing \(1987\)](#), causing the nebula to have low excitation. We propose that this structure might have been originated by a late thermal pulse event experienced by HD 826, which also turned it into a [WC]-type star. This would make NGC 40 a member of the unpopulated group of born-again PNe.

Future high-resolution mid- and far-IR images and spectra will be pursued and will be used to produce a complete modelling of NGC 40. This will help characterise these structures and shed light into their origin.

ACKNOWLEDGEMENTS

The authors are thankful to R.L.M. Corradi for providing the INT nebular images of NGC 40 and to W. Henney for fruitful discussion. JAT, MAG and HT are funded by UNAM DGAPA PAPIIT project IA100318. GRL acknowledges support from Fundación Marcos Moshinsky, CONACyT and PRODEP (Mexico). MAG acknowledges support of the grant AYA 2014-57280-P, cofunded with FEDER funds. This work has made extensive use of the NASA's Astrophysics Data System. This work uses public data from the IR telescopes *Spitzer* and *Herschel* through the NASA/IPAC Infrared Science Archive, which is operated by the Jet Propulsion Laboratory at the California Institute of Technology, under contract with the National Aeronautics and Space Administration. This paper also presents data obtained with WIRC*am*, a joint project of CFHT, Taiwan, Korea, Canada, France, and the Canada-France-Hawaii Telescope (CFHT) which is operated by the National Research Council (NRC) of Canada, the Institut National des Sciences de l'Univers of the Centre National de la Recherche Scientifique of France, and the University of Hawaii.

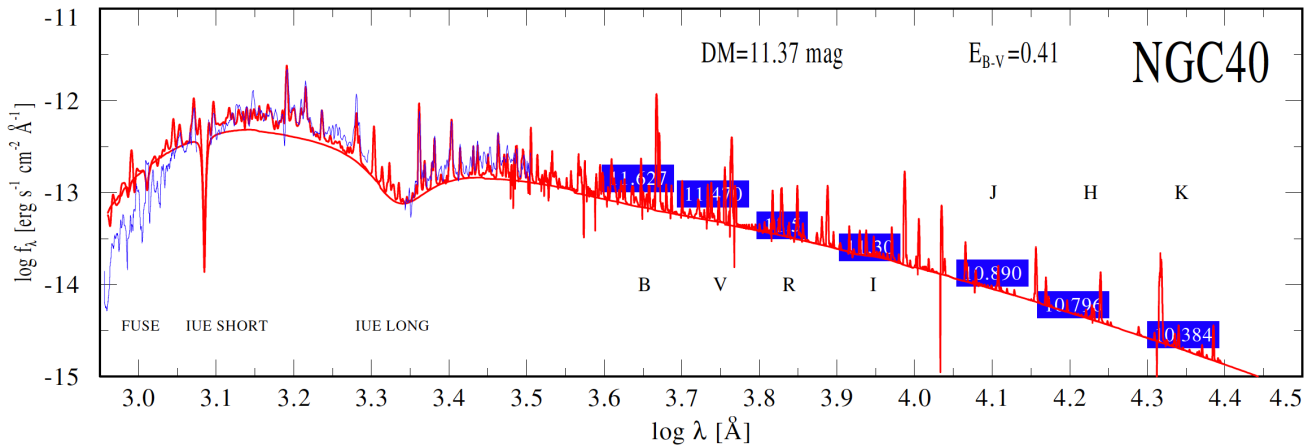


Figure 10. Spectral Energy Distribution (SED) of HD 826 from the UV to the IR range. Blue squares are photometric measurements in the indicated bands. The SED obtained for our best-fit model is shown in red.

- MNRAS, 456, L89
- Evans, A., Tyne, V. H., van Loon, J. T., et al. 2006, MNRAS, 373, L75
- Fang, X., Guerrero, M. A., Marquez-Lugo, R. A., et al. 2014, ApJ, 797, 100
- Ferland, G. J., Chatzikos, M., Guzmán, F., et al. 2017, Rev. Mex. Astron. Astrofis., 53, 385
- Forrest, W. J., Houck, J. R., & McCarthy, J. F. 1981, ApJ, 248, 195
- Frew, D. J. 2008, Ph.D. Thesis, Maquarie University
- Gräfener, G., Koesterke, L., & Hamann, W.-R. 2002, A&A, 387, 244
- Guerrero, M. A., Fang, X., Miller Bertolami, M. M., et al. 2018, Nature Astronomy, 2, 784
- Guerrero, M. A., Ruiz, N., Hamann, W.-R., et al. 2012, ApJ, 755, 129
- Guerrero, M. A., & De Marco, O. 2013, A&A, 553, A126
- Guzmán-Ramírez, L., Lagadec, E., Jones, D., Zijlstra, A. A., & Gesicki, K. 2014, MNRAS, 441, 364
- Guzmán-Ramírez L., Zijlstra A. A., Níchuimín R., Gesicki K., Lagadec E., Millar T. J., Woods P. M., 2011, MNRAS, 414, 1667
- Hamann, W.-R., & Gräfener, G. 2004, A&A, 427, 697
- Harman, R. F., & Seaton, M. J. 1966, MNRAS, 132, 15
- Hamann, W.-R., & Koesterke, L. 1998, A&A, 335, 1003
- Herwig, F. 2005, ARA&A, 43, 435
- Herwig, F. 2001, Ap&SS, 275, 15
- Hillier, D. J. 1991, A&A, 247, 455
- Kameswara Rao, N., Sutaria, F., Murthy, J., et al. 2018, A&A, 609, L1
- Kim, H., Trejo, A., Liu, S.-Y., et al. 2017, Nature Astronomy, 1, 0060
- Köppen, J., & Tarafdar, S. P. 1978, A&A, 69, 363
- Leuenhagen, U., Hamann, W.-R., & Jeffery, C. S. 1996, A&A, 312, 167
- Marcolino, W. L. F., Hillier, D. J., de Araujo, F. X., & Pereira, C. B. 2007, ApJ, 654, 1068
- Martin, J., Xilouris, K., & Soker, N. 2002, A&A, 391, 689
- Meaburn, J., Lopez, J. A., Bryce, M., & Mellema, G. 1996, A&A, 307, 579
- Miller Bertolami, M. M., & Althaus, L. G. 2007, A&A, 470, 675
- Monteiro H., Falceta-Gonçalves D., 2011, ApJ, 738, 174
- Montez, R., Jr., Kastner, J. H., De Marco, O., & Soker, N. 2005, ApJ, 635, 381
- Mishra, A., Li, A., & Jiang, B. W. 2015, ApJ, 802, 39
- Pottasch, S. R., Bernard-Salas, J., Beintema, D. A., & Feibelman, W. A. 2003, A&A, 409, 599
- Preite-Martinez, A., & Pottasch, S. R. 1983, A&A, 126, 31
- Ramos-Larios, G., Vázquez, R., Guerrero, M. A., et al. 2012, MNRAS, 423, 3753
- Ramos-Larios, G., Phillips, J. P., & Cuesta, L. C. 2011, MNRAS, 411, 1245
- Ramos-Medina, J., Sánchez Contreras, C., García-Lario, P., et al. 2018, A&A, 611, A41
- Schmutz, W., Hamann, W.-R., & Wessolowski, U. 1989, A&A, 210, 236 q
- Seaton, M. J. 1979, MNRAS, 187, 73P
- Sloan, G. C., Lagadec, E., Zijlstra, A. A., et al. 2014, ApJ, 791, 28
- Sloan, G. C. 2017, Planet. Space Sci., 149, 32
- Smith, J. D. T., Armus, L., Dale, D. A., et al. 2007, PASP, 119, 1133
- Toalá, J. A., Guerrero, M. A., Todt, H., et al. 2015, ApJ, 799, 67
- Todt, H., & Hamann, W.-R. 2015, Proceedings of the Wolf-Rayet Stars Workshop (Potsdam, Germany), eds. Wolf-Rainer Hamann, Andreas Sander, and Helge Todt. Universitätsverlag Potsdam, 253
- Todt H., Sander A., Hainich R., Hamann W.-R., Quade M., Shenar T., 2015, A&A, 579, A75
- Zhang, Y., & Liu, X.-W. 2005, ApJL, 631, L61